ACS OMEGA

http://pubs.acs.org/journal/acsodf

Article

Fabrication of γ-Al_2O_3 Nanoarrays on Aluminum Foam Assisted by Hydroxide for Monolith Catalysts

Shengpan Peng,[§] Ziran Ma,[§] Jing Ma, Zhihua Han, Hongyan Wang, Baodong Wang,* Feng Zhao, and Ge Li

Cite This: *ACS Omega* 2023, 8, 1643−1651

Read Online

ACCESS | Metrics & More | Article Recommendations | Supporting Information

ABSTRACT: Heat distribution and good adhesion of the washcoat on monolith catalysts are critical to improving catalytic activity and long-term stability. Compared with cordierite, metal foam presents a high thermal conductivity coefficient. Also, the availability of "washcoat" *in situ* grown on metal substrates opens the door to eliminating the problem of coating peeling. Generally, hydrothermal or thermal methods are used for the fabrication of *in situ* grown washcoat on metal substrates. In this research, the aluminum foam monolith vertically aligned Al_2O_3 nanowire array is successfully prepared at ambient temperature in an alkaline solution for the first time. Furthermore, the Pt-loaded Al_2O_3 nanowire array (0.5 $g_{Pt}/L_{monolith}$) is applied to C_2H_4 degradation. The catalyst converts 90% C_2H_4 at 147 °C with a gas hourly space velocity (GHSV) of 20,000 h^{-1}. And a little decrease (1%) is observed in catalytic activity, even in 15 vol % water vapors. The catalysts show good thermal stability and water resistance property over 36 h at 300 °C. Above all, this study presents a simple way of *in situ* growth of washcoat on metal-substrate monolith with potentially scaled manufacturing. And the monolith catalyst shows good catalytic performance on C_2H_4, which can be applied for volatile organic compound treatment.

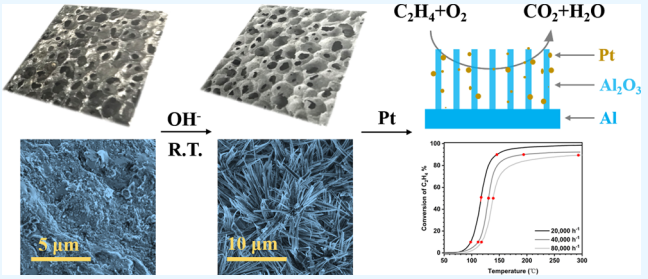

1. INTRODUCTION

The increasing frequency of haze pollution in China has drawn widespread attention as a result of fast and energy-intensive growth over the last several decades. The implementation of China's toughest-ever clean air policy results in a significant reduction in SO_2, NO_x, CO, and volatile organic compound (VOC) concentrations. VOCs also contribute significantly to global warming as reported by the Intergovernmental Panel on Climate Change (IPCC) Fifth Assessment Report in 2013.[1] VOC emissions are still primarily caused by industrial processes and solvent use.[2] Many recovery technologies (such as adsorption, absorption, membrane separation, and condensation) and oxidative approaches, such as catalytic oxidation (CO), thermal incineration (TO), biological degradation, photocatalytic decomposition, and nonthermal plasma oxidation, have been developed to reduce VOC emissions.[3] CO, which decomposes VOC pollutants over suitable monolith catalysts at much lower temperatures (typically 200−500 °C) compared to TO,[3] is one of the most effective and economically feasible technologies to eliminate dilute VOC (<0.5 vol %) effluent streams.

Ceramics made from synthetic cordierite ($2MgO{\cdot}2Al_2O_3{\cdot}5SiO_2$) are typically employed as monoliths because of their resilience under vibration and attrition, as well as at high temperatures (>1000 °C).[4−6] Pt, Pd, or Rh is generally supported on the high surface area γ-Al_2O_3 and then placed on the walls of the cordierite.[7,8] Long-term performance in widely variable exhaust gas circumstances requires good washcoat adherence to the substrate. The catalytic oxidation device functions on alternate cycles of heat storage and release of regenerative beds, resulting in the oscillation temperature of monolith catalysts, which results in easy adhesion between the washcoat and the substrate due to the variable coefficient of thermal expansion. Furthermore, the difference in heat conductivity coefficients between cordierite (~0.06 W m^{-1} K^{-1}) and γ-Al_2O_3 (~20 W m^{-1} K^{-1}) promotes washcoat peeling.[9] The reaction is fast and the conversion is regulated by mass transfer when the conversion efficiency is high.[10] It is effective at improving mass transfer to the catalyst by increasing the catalyst quantity and using a high-cell density substrate (with a larger contact area and smaller cell width).[10,11] However, smaller substrate channel diameters are associated with larger diffusion boundary layers and higher pressure drop.[12,13] Furthermore, the typical coating process results in a nonuniform surface topography, which renders the

Received: November 10, 2022
Accepted: December 20, 2022
Published: December 28, 2022

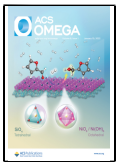

https://doi.org/10.1021/acsomega.2c07237
ACS Omega 2023, 8, 1643−1651

catalyst more susceptible to inactivation.[14] As noted above, the deficiencies of cordierite clearly reduce the activity and longevity of the supported catalysts.

Metal substrates can be covered by a "washcoat" with *in situ* growth, resulting in greater adhesion between substrates and overlayer due to chemical linkages. Open-cell metal substrates, for example, have been proposed for the removal of gaseous pollutants,[14−17] water treatment,[18,19] reforming of methane,[20] supercapacitors,[21] fuel cells,[22] thermal storage,[23] and so on. Furthermore, the coefficient of thermal conductivity of metals such as Al (~237 W m^{-1} K^{-1}) is hundreds of times greater than that of cordierite, resulting in more uniform temperature distribution and improved heat efficiency when employed on a broad scale. Furthermore, as illustrated in Table 1 and Figure 1, metal-foam-based catalysts have an interconnected three-dimensional channel structure that improves gas mass transfer.[16] Moreover, metal substrates provide an applicable way to heat monolith catalysts with electricity. Electrical power applied to electrified conductive monolithic metal-based catalysts on monolith can cause the release of lattice oxygen from the catalyst, resulting in much lower reaction temperatures.[24] As a result, metal foam-based monolithic catalysts will be a viable option. As is well known, hydrothermal or thermal methods are used to prepare open-cell metal substrates for *in situ* generated washcoat.[14,15,18] However, neither hydrothermal nor thermal methods can easily prepare the monolithic catalyst at lower temperatures and offer the probability of scalable production.

Table 1. Characteristics of Cordierite and Al Foam

	Al foam	cordierite
thermal conductivity	237 W m^{-1} K^{-1}	0.06 W m^{-1} K^{-1}
pore structure	3 dimensions	1 dimension
coating process	one step	several steps
washcoat−monolith interaction	chemical	physical
heat distribution	even[14]	not even[12,25]

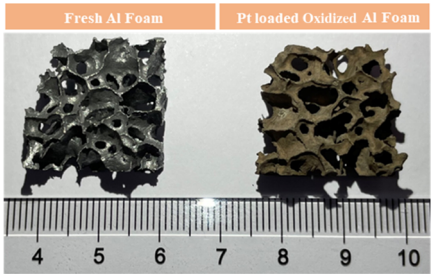

Figure 1. Photo of fresh and synthesized aluminum foam. Photograph courtesy of Shengpan Peng. Copyright 2022.

We discuss here the fabrication of γ-Al_2O_3 nanowire arrays on open-celled aluminum foam (denoted as OAl-foam) by impregnation in the alkaline solution at room temperature, as well as the performance of Pt-loaded OAl-foam for C_2H_4 catalytic oxidation. In comparison to the existing synthetic approaches, this study presents a simple way of producing monolithic catalysts with potential applications in manufacturing. Interestingly, the exposed crystal planes of the triangular prism-shaped γ-Al_2O_3 nanowires are $(10\bar{1})$, $(\bar{1}12)$, and $(\bar{1}2\bar{1})$. Compared with γ-Al_2O_3 facets containing (100), (101), or (111) facets,[26,27] the exposed triangular prism-shaped γ-Al_2O_3 facets have higher surface energies for strongly attaching Pt,[28] consequently disseminating Pt active phase uniformly. The loaded noble metal evenly spreads as small nanoparticles (<4 nm) or single atoms on γ-Al_2O_3 of aluminum foam. Catalytic combustion of C_2H_4 is chosen as a probe experiment to assess the activity of the VOC oxidation catalysts. At 147 °C, the catalyst converts 90% C_2H_4 at a rate of 20,000 h^{-1}. Water vapor (15 vol %) has little effect on C_2H_4 catalytic activity. As a result, this study proposes a simple and effective approach for creating a hierarchical γ-Al_2O_3 framework that may be employed as a monolith catalyst in VOC treatment due to its chemical adhesion, activity, thermal stability, and water resistance.

2. EXPERIMENTAL SECTION

2.1. Materials. An open-cell aluminum foam monolith from Shanghai Yinfu with <5 mm pores (~60 cpi) was cut to obtain a mini-monolith (2.0 cm × 2.0 cm × 0.9 cm; 0.30 g cm^{-3}) with a mass of ~1.1 g. $Pt(NO_3)_2{\cdot}2H_2O$ (15% as Pt) was purchased from Shanghai Jiuling Chemical Co., Ltd.. NaOH was purchased from Sinopharm Chemical Reagent Co., Ltd.

2.2. Preparation of the Monolith Catalyst. First, deionized water was used to ultrasonically clean the open-cell aluminum foam components. After that NaOH powder was dissolved in deionized water to obtain a solution with a pH of 12 and the solution temperature is 40 °C. Next, the cleaned aluminum foam pieces were added to the solution and a large number of bubbles were created in the solution. The oxidized aluminum foam was removed after 4 h, rinsed, and dried in an oven (at 120 °C). The monolithic catalyst was then created by impregnating aluminum foam with a $Pt(NO_3)_2$ aqueous solution. Pt loading in aluminum foam was 0.5 g of Pt per liter. At 50 °C, the loaded Pt-solution aluminum foam was evaporated for 12 h. The finished products were calcined in air at 550 °C for 5 h using a 5 °C min^{-1} heating ramp.

2.3. Monolith Characterization. X-ray diffraction (XRD, Bruker D8 ADVANCE) with monochromatic Cu Kα radiation was used to evaluate the phase purity and crystal structure of the catalysts. To explore surface morphology and elemental analysis on the catalyst interface, an FEI scanning electron microscope (SEM, Nova NanoSEM 450) equipped with an energy dispersive spectroscopy (EDS) detector was utilized to capture high-resolution pictures. Transmission electron microscopy (TEM) images were taken using a JEM-ARM200F (JEOL) at a voltage of 200 kV. After dispersing a limited number of samples in ethanol, the solution was placed on a carbon-coated Cu grid and dried at room temperature.

2.4. Reaction System and Activity Measurements. All of the tests were carried out under atmospheric pressure. Experiments with ethylene (C_2H_4) oxidation were carried out in a micro-reactor with an internal diameter of 30 mm. The volume of the catalyst was 21.6 mL (six pieces of mini-monolith). An oven was used to heat the reactor, and the temperature of the catalyst was monitored using a K-type thermocouple placed within the reactor and close to the catalytic bed. When just the bare supports were inserted in the reactor at temperatures utilized for kinetics tests, no discernible conversions were seen. The composition of the reactant mixture was adjusted by adjusting the flow rates of C_2H_4 (700 ppm), O_2 (20 vol %), and N_2 while keeping the overall flow rate constant at 800 L h^{-1}. The parameters were consistent with a GHSV (gas hourly space velocity) of 40,000 h^{-1}. The

https://doi.org/10.1021/acsomega.2c07237
ACS Omega 2023, 8, 1643−1651

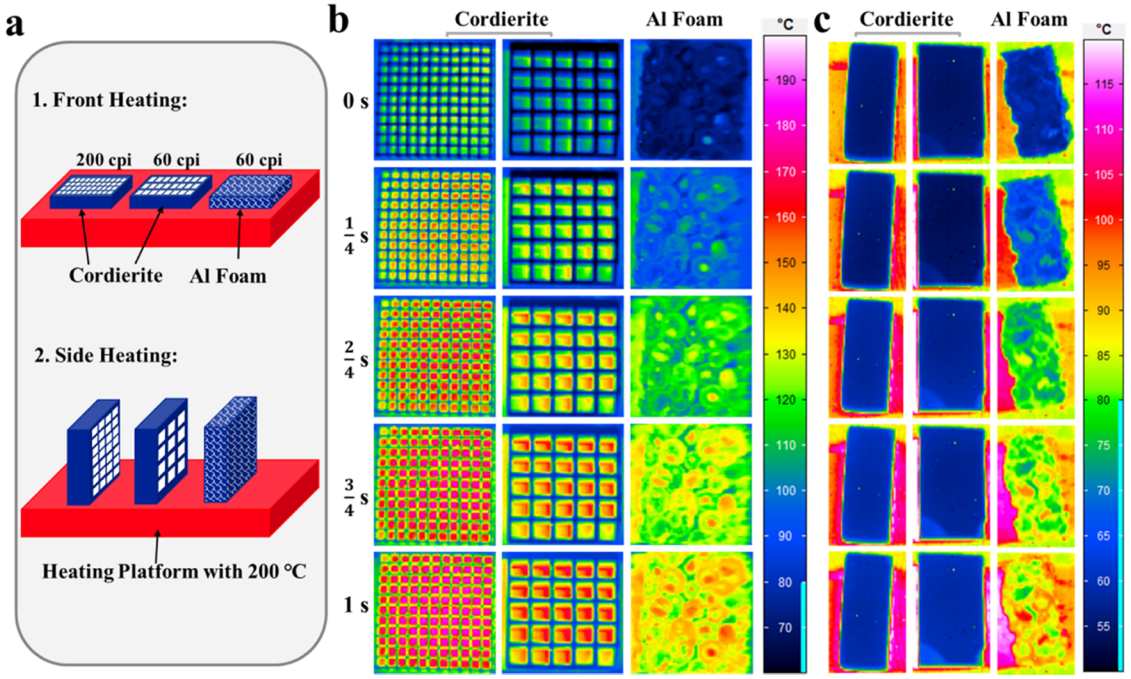

Figure 2. (a) Scheme of heating methods of monolith substrates. Infrared thermal images of cordierite and Al foam (b and c).

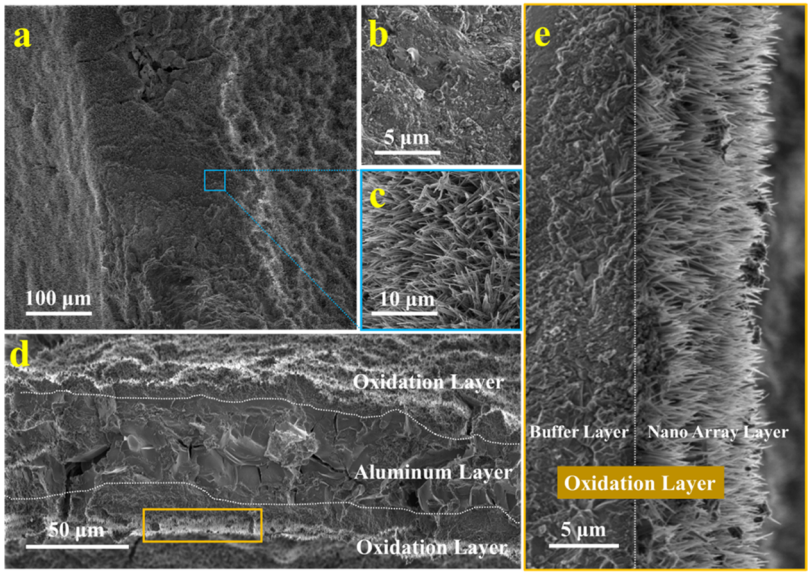

Figure 3. SEM images of fresh Al foam and oxidized Al foam. (a) Surface structure of oxidized Al substrates; (b) surface structure of fresh Al substrates; (c) enlarged view inside the light blue box in (a); (d) sectional view of the oxidation Al substrates, and (e) enlarged view inside the gold box in (d).

operating pressure was one atmosphere, and the pressure drop (0.015 atmosphere) was ignored. A Fourier transform infrared (FT-IR) gas analyzer (MKS, MultiGas analyzer, model 6030) equipped with a liquid-nitrogen cooled mercury−cadmium−telluride (MCT) detector was used to monitor the composition of the effluent gases in real-time. The water resistance of the catalysts was evaluated at a temperature that achieved 90 percent ethylene conversion in the dry phase. The reaction gas was then blended with water vapor by heating ultrapure water injected with a precision syringe. After some time, the injected water vapor was turned off, and the concentration of ethylene was measured throughout the process. The catalysts were tested for 36 h to determine their stability.

3. RESULTS AND DISCUSSION

3.1. Heat Distribution. To evaluate heat distribution on cordierite and Al foam, surface infrared thermal analysis is performed for 200 cpi monolith cordierite, 60 cpi monolith cordierite, and 60 cpi Al foam, as shown in Figure 2. Two types of heating methods are shown in Figure 2a. The samples are placed on a heating platform at a constant temperature of 200 °C, and pictures of infrared thermal imaging in various phases are shown in Figure 2b,c. The surface temperature of Al foam rises the fastest and has the most uniform temperature field

https://doi.org/10.1021/acsomega.2c07237
ACS Omega 2023, 8, 1643−1651

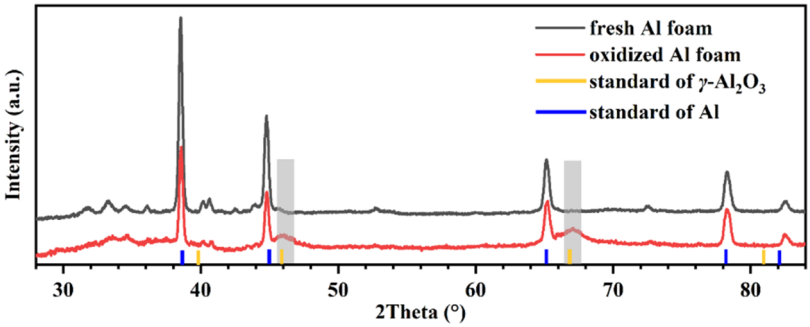

Figure 4. XRD patterns of Al foam before and after oxidation.

distribution. In addition, the surface temperature (~140 °C) of Al foam is closer to the heating temperature (200 °C) after only 1 s in Figure 2b. In the same time period, though thermal convection in the channels promptly increases the surface temperature of walls (~120 °C), the temperature of the medium layer of cordierite walls is only around 70 °C. The temperature difference would lead to washcoat peeling because of different thermal expansion between substrates and washcoat. Furthermore, to eliminate the thermal convection in channels, the temperature increase is observed by side heating in Figure 2b. The surface temperature of Al foam increases to 100 °C after 1 s, while 200 cpi monolith cordierite and 60 cpi monolith cordierite take 1 s to reach 60 °C, respectively. This result shows the superior thermal performance of Al foam, which can be attributed to its higher thermal conductivity compared to cordierite.

3.2. Monolith Characterization. Figure 1 shows photographs of virgin and oxidized Al foam, a framework composed of open cells (≤5 mm) is observed. Figure 3a shows a low-magnification SEM view of the fluffy material (Al_2O_3) spreading uniformly across oxidized Al substrates. Fresh Al substrates (Figure S1) already have a thick and slightly rough aluminum surface. To confirm the details of the Al substrate surface, high-magnification SEM pictures (Figure 3b) show no flaws, such as fractures, cavities, or heaves. The naturally formed oxide film (amorphous Al_2O_3) on aluminum increases extremely slowly and remains nearly constant in time with a thickness of 3 nm.[29,30] It protects the metal surface from further deterioration. The SEM picture in Figure 3c shows that nanowire arrays with triangular prism shapes are formed vertically on oxidized Al substrates, roughly 10 μm long and 250 nm wide (Figure S2). The central area of the cross-section in Figure 3d exhibits significantly more metallic shine than the sides, showing that the primary component inside the oxidized Al substrates can be mainly metallic Al. And Figure S3 shows EDS pictures of a cross-section of an oxidized Al substrate, demonstrating that the major component of the Al foam is still aluminum. As illustrated in Figure 3d, the oxidized layer is approximately 20 μm thick, which is much thinner than the washcoat (50−100 μm) on cordierite. Figure 3e (enlarged view of Figure 3d) shows an Al_2O_3 nanowire array on the buffer layer with a thickness of several microns. The buffer layer on metallic Al is loose, porous, and much thicker than the naturally dense passivation oxidation layer.

The XRD pattern of fresh Al foam (Figure 4) clearly shows a single phase with diffraction peaks (38.5, 44.7, 65.1, and 78.2°) pertaining to the cubic Al phase (PDF 04-0787). Because the thickness of the amorphous oxide layer is just a few nanometers, any distinctive peaks of Al_2O_3 cannot be observed on fresh Al foam in the pattern. XRD measurements are also performed on oxidized Al foam to determine the phase composition and crystallographic characteristics. The XRD pattern in Figure 4 confirms that γ-Al_2O_3 is produced by the oxidation of aluminum in an alkaline solution. Two peaks at 46 and 67° (in the gray strips), corresponding to the (200) and (220) planes of γ-Al_2O_3 nanowires, are much weaker than those of the standard PDF 75-0921 card, indicating the small amount of γ-Al_2O_3.

Figure 5a shows a high-angle annular dark-field (HAADF) scanning transmission electron microscopy (STEM) picture of

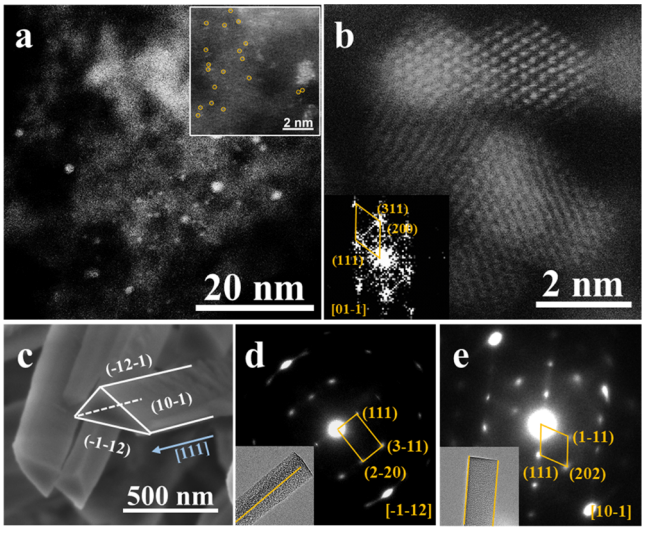

Figure 5. (a) and (b) High-resolution STEM images of 0.5 $g_{Pt}/L_{oxide\ Al\ foam}$, inset of (a) is single-atom Pt, inset of (b) is the selected area electron diffraction (SAED) of Pt nanoparticles; (c) SEM images of γ-Al_2O_3 nanowires of oxide Al foam; and (d) and (e) selected area electron diffraction (SAED) of γ-Al_2O_3 nanowires, and TEM images (inset) of individual γ-Al_2O_3 nanowire of oxide Al foam.

Pt dispersion on the γ-Al_2O_3 surface. The typical picture demonstrates the formation of extremely tiny Pt particles (less than 4 nm) on the γ-Al_2O_3 support, even after calcination at a high temperature (550 °C) for hours. The inset of Figure 5a shows the atomic dispersion of Pt on the γ-Al_2O_3 surface. Table S1 shows the elemental quantitative analysis performed by EDS in this investigation. Almohamadi et al.[6] coated powder catalysts with 1.23 $g_{Pd}/L_{monolithic\ catalyst}$ on the cordierite monolith, just 1.5 wt % Pd on the surface of the washcoat layer was observed. The washcoat offers a vast surface area for the chemical reaction on cordierite monoliths; nevertheless, diffusion resistances in the washcoat lead to decreased reaction

https://doi.org/10.1021/acsomega.2c07237
ACS Omega 2023, 8, 1643−1651

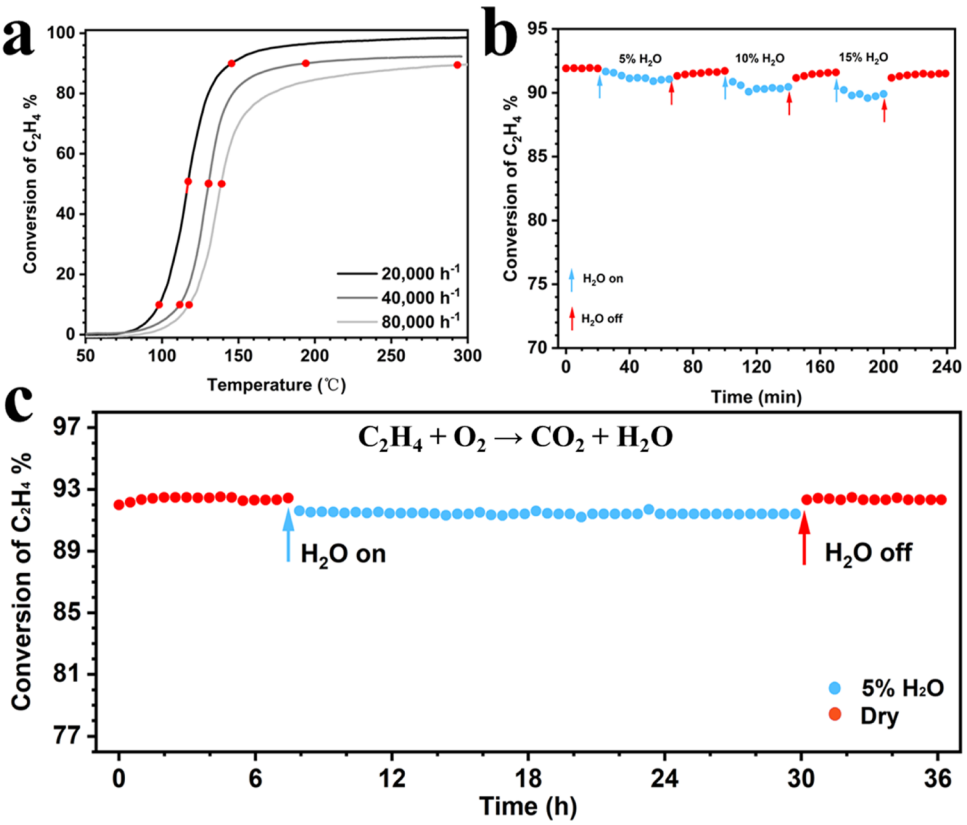

Figure 6. Catalysts activity and stability (C_2H_4 700 ppm, O_2 20%, N_2 balance). (a) Catalysts activity at different gas hourly space velocity; (b) water resistance of Pt-loaded on oxide Al foam under conditions of 40,000 h^{-1} at 300 °C; and (c) thermal stability of Pt loaded on oxide Al foam in a 36 h stream under conditions of 40,000 h^{-1} at 300 °C.

rates.[12,16] Despite the fact that the loading is 0.5 $g_{Pt}/L_{oxidation\ Al\ foam}$ in this study, the EDS analysis results reveal 6.4 wt % Pt on the surface of Al foam. It means Pt is equally disseminated on the surface of the Al foam washcoat, which could reduce the diffusion resistance.

The HAADF-STEM and selected area electron diffraction (SAED) patterns in Figure 5b proves the presence of metallic Pt nanoparticles on γ-Al_2O_3. The morphology of γ-Al_2O_3 nanowires is investigated on alumina supports (Figure 5c–e). The SEM picture (Figure 5c) reveals triangular prisms of γ-Al_2O_3 nanowires grown vertically with flat surfaces in lengths and top. Every side of the triangle is less than 250 nm in width. SAED of individual γ-Al_2O_3 nanowires is detected to get crystal face indices (Figure 5d,e). The three sides of the right-angled triangular prism γ-Al_2O_3 nanowire are $(\bar{1}\bar{1}2)$, $(10\bar{1})$, and $(\bar{1}2\bar{1})$ and the growth direction is [111]. γ-Al_2O_3 oxides are generated by the thermal dehydration of aluminum hydroxides and oxyhydroxides.[31−33] In particular, boehmite (γ-AlOOH) is the starting material for the manufacture of the γ-Al_2O_3 catalytic support.[33,34] There have been publications on the shape control of γ-Al_2O_3 facets contained by the (100), (101), and (111) facets in the form of nanorods, nanoflakes, nanowires, and so on.[35−37] So far, nanocrystals γ-Al_2O_3 with higher index facets are rarely reported. Through hydroxide catalysis, a right-angled triangular prism γ-Al_2O_3 nanowire encompassed by $(\bar{1}\bar{1}2)$ and $(\bar{1}2\bar{1})$ higher index facets is successfully synthesized in this work. In the case of face-centered cubic (fcc), high-index planes are open-structure surfaces with a high density of atomic steps and kinks, characterized by a set of Miller indices (hkl) with at least one index greater than unit.[38,39] γ-Al_2O_3 nanowires have face-centered cubic unit cells. Exposed $(\bar{1}\bar{1}2)$ and $(\bar{1}2\bar{1})$ facets have a higher density of atomic steps and kinks than (100), (101), and (111) facets, facilitating metal–support interactions. Kwak et al.[40] discovered that coordinatively unsaturated Al^{3+} centers on the (100) facets of the γ-Al_2O_3 support would atomically anchor Pt with Pt–O bonds. The $(\bar{1}\bar{1}2)$ and $(\bar{1}2\bar{1})$ facets may expose much more low-coordinated Al atoms. These low-coordinated atoms can interact aggressively with supported noble metals or function as active sites for chemical bond breakdown,[36] as shown in Figure 5a inset. As a result, a high fraction of high-energy exterior surfaces may be beneficial for high catalytic performance.

3.3. Catalysts Activity and Stability. For C_2H_4 catalytic oxidation, Pt-loaded oxidized Al foam (Pt/OAl) is effectively created. The C_2H_4 conversion temperature value of the Pt/OAl monolithic catalyst is much lower than that of the Pt-loaded fresh Al foam (Pt/Al) monolithic catalyst (Figure S4). Under the same test conditions, Pt/Al conversion temperatures at 10% (T_{10}) is 200 °C, which is around 90 °C higher than that of Pt/OAl. Furthermore, Figure 6a is the light-off curves of Pt/OAl at various GHSV levels (20,000, 40,000, and 80,000 h^{-1}), the detailed results are displayed in Table 2. Although the rise in T_{90} values with increasing GHSV levels is clearly visible in Figure 6a and Table 2, T_{90} is less than 300 °C even at 80,000 h^{-1}. The catalytic activity of the prepared Pt-loaded cordierite and Pt/OAl monolithic catalysts was evaluated for the total oxidation of C_2H_4 as shown in Table 3. When the GHSV is close to real operating conditions (20,000 h^{-1}), T_{50} and T_{90} of Pt/OAl are 117 and 147 °C,

https://doi.org/10.1021/acsomega.2c07237
ACS Omega 2023, 8, 1643−1651

Table 2. Catalysts Activity at Different Gas Hourly Space Velocity

parameters	20,000 h^{-1}	40,000 h^{-1}	80,000 h^{-1}
T_{10} (°C)	98	112	118
T_{50} (°C)	117	131	138
T_{90} (°C)	147	196	292

Table 3. Catalysts Activity with Different Support at 20,000 h^{-1}

support	T_{10} (°C)	T_{50} (°C)	T_{90} (°C)
cordierite	179	190	310
Al foam	98	117	147

respectively. The Pt-loaded cordierite with the same pore size and Pt loading as Pt/OAl shows poor catalytic performance. These findings imply that Pt/OAl monolith catalysts can significantly increase catalytic conversion efficiency compared to Pt/Al and meet the practical application scenario conditions (like exhaust gas treatment of vinyl silo). Above all, the formation of the γ-Al_2O_3 nanowire array over the Al foam contributes to the improved catalytic activity.

Moreover, water resistance is an important sign of catalyst suitability. C_2H_4 conversion on Pt/OAl is measured at 300 °C in the presence of 5, 10, and 15 vol % water vapor (Figure 6b). The C_2H_4 conversion is reduced from 92.0 to 91.2, 90.3, and 89.6%, respectively. These results clearly show that water vapor has little effect on C_2H_4 oxidation activity. The activity of catalysts coated on cordierite is substantially more sensitive to water vapor,[6,14] owing to capillary condensation of water in catalyst nanopores.[41] The washcoat on cordierite is constructed by powder with an abundance of pores, in which water undergoes a gas-to-liquid phase transition due to confinement induction. On one hand, liquid water will clog pores and impede mass transport. Active sites will be covered, on the other hand, resulting in reversible inactivation. However, with the exception of the nanowire array, there are essentially no nanopores on the oxidized Al foam, which basically inhibits catalyst reversible deactivation caused by capillary condensation water. The thermal and hydrothermal stability of these catalysts is also critical in real-world applications. The catalytic performances of Pt/OAl for C_2H_4 degradation are tested for 36 h under dry and humid circumstances (5 vol %) at 300 °C (Figure 6c). Figure 6c demonstrates that the C_2H_4 conversion varies little in dry or humid circumstances at 300 °C, indicating that the Pt/OAl monolithic catalyst maintains high stability. Specially, C_2H_4 conversion is 93% without water in the first 6 h. After injecting 5 vol % water vapor, the C_2H_4 conversion decreases to 91% and remains steady during the next 13 h. And then the C_2H_4 conversion efficiency is recovered with no declining trend after turning off the water vapor. Finally, after the stability test, the nanoarray morphology of the Pt/OAl monolith does not change according to SEM (Figure S5).

3.4. Growth Mechanism of γ-Al_2O_3 Nanowires over the Substrate. A putative physicochemical mechanism is presented to explain the interaction of Al foam with an alkaline solution. The dense oxidation layer formed in air on fresh Al foam is difficult to be removed as shown in Scheme 1 (Stage 0). Under alkaline circumstances, hydration of the oxidation layers largely involves the hydrolysis of Al−O−Al bonds to create Al−OH species.[42] Extensive hydration eventually results in oxyhydroxide or hydroxide phases such as AlOOH and

Scheme 1. Assumption Diagram of Nanowire Growth Mechanism

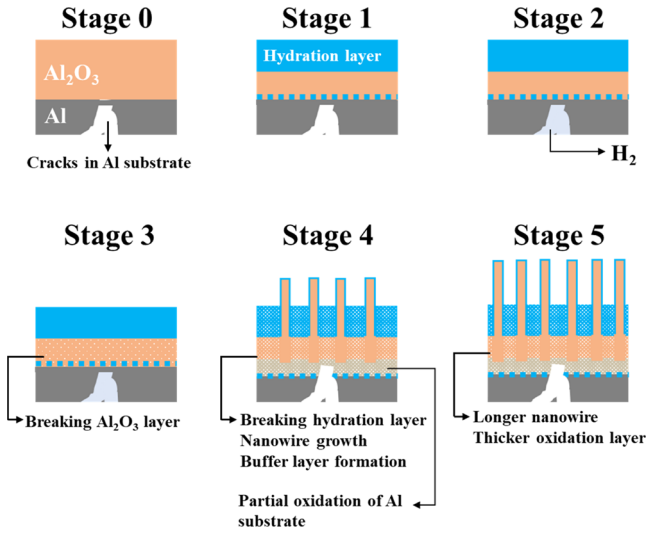

$Al(OH)_3$, which are thermodynamically more stable at room temperature than Al_2O_3. And then, the mobile species in the Al_2O_3 layer are OH^- ions (or H_2O molecules), and their transport rates are fast enough to account for the kinetics of the Al corrosion process ($AlOOH + Al \rightarrow Al_2O_3 + H_2$) at the interface of Al and Al_2O_3 (Stage 1).[43] These stages can be supported by XPS analysis. To confirm the surface components of the oxide layer on Al foam, as well as their valence states, further analysis by XPS was carried out. As Figure 7a illustrates, Al 2p spectra fitted by a Lorentzian−Gaussian display three significant peaks, where one, located at the binding energy of 73.7 eV, is attributed to the oxidation layer on fresh Al foam, the second one, centered at 70.9 eV, indicates the existence of Al metal, and the last one, centered at 71.4 eV, indicates the existence of transition state $Al^{\delta+}$ ($0 < \delta < 3$) at the junction of thin oxidation layer and Al metal. In light of the information obtained from Figure 7b, the O 1s XPS spectra of fresh Al foam exhibit dual peaks for different oxygen species. The main peaks denoted as O_{lat}. at 530.9 eV elucidate the lattice oxygen on the oxidation layer surface, while the shoulder peaks denoted as O atom linked to $Al^{\delta+}$ ($O\text{-}Al^{\delta+}$) at a lower binding energy of 529.0 eV. As a comparison, Al 2p (Figure 7c) and O 1s (Figure 7d) of oxidized Al foam show different XPS spectra. First, the peak of metal Al vanished because of the oxidation of Al and the generation of a thick oxidized layer. Second, detected Al−OH species suggest that the hydration of the oxidation layers leads to the hydrolysis of Al−O−Al bonds. And then the Al corrosion process ($AlOOH + Al \rightarrow Al_2O_3 + H_2$) at the interface of Al and Al_2O_3 occurred kinetically.

In stage 2, when the tensile strength of the dense oxidation layer and the atmospheric pressure surpasses H_2 bubbles pressure, H_2 bubbles spontaneously generate at the Al−Al_2O_3 interface and fill between the interface, leading to the prohibitive corrosion reaction ($AlOOH + Al \rightarrow Al_2O_3 + H_2$).[44,45] In the Al foam, H_2 bubbles can flow from the interface into fractures in Al substrates because of the lower tensile strength at the position of inside cracks (as shown in Figure S1), which promotes the $AlOOH + Al \rightarrow Al_2O_3 + H_2$ reaction. In stage 3, the produced Al_2O_3 shows increased phase volume compared to Al, decreasing the tensile strength of the

https://doi.org/10.1021/acsomega.2c07237
ACS Omega 2023, 8, 1643−1651

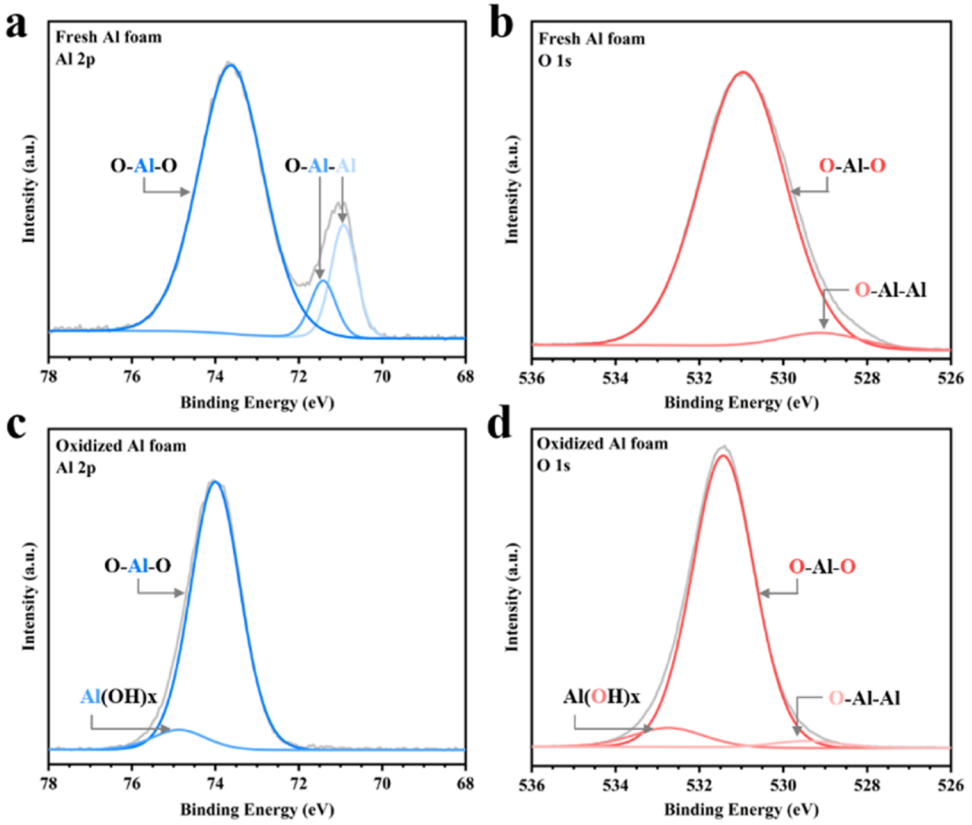

Figure 7. XPS spectra of fresh Al foam and oxidized Al foam: (a) and (c) Al 2p and (b) and (d) O 1s.

dense oxidation layer, and more hydrogen production raises the internal gas pressure. Until the oxidation layers are broken into particles (as shown in Figures S7 and S8), the specific structure (nanoarray) of Al_2O_3 starts to grow on the buffer layer (Stage 4). The rough cross-section in Figure 8, for example, provides evidence that the oxidation layer is smashed into small grains. The porous oxidation layer and buffer layer, as shown in Figure 3e, ensure that Al will react with water continually.[46,47] Furthermore, the nanowires grow longer with time, while the width remains constant in stage 5. Specially, when the reaction time is long enough, nanowires will form bundles as shown in Figure 8c. These observations indicate that the nanoarray may be formed by the production of grains in the buffer layer. The Al/Al_2O_3 in the buffer layer transfers to Al_2O_3 and produced H_2, requiring more space. The gap formed between adjacent particles facilitates the flow of H_2, which hinders the migration of Al ions between Al_2O_3 particles, resulting in the growth of generated Al_2O_3 in a specific direction with a structured framework. The increased reaction temperature causes H_2 bubbles to overflow with smaller sizes, creating smaller grains, and forming crossing ribbon nanoarrays with thickness of tens of nanometers, as illustrated in Figure 8d. The structural alteration can be described by the depicted process in Scheme 1. The phenomena of γ-Al_2O_3-modified Al constantly reacting with pure water and producing hydrogen at ambient temperature and atmospheric pressure have been thoroughly studied.[47]

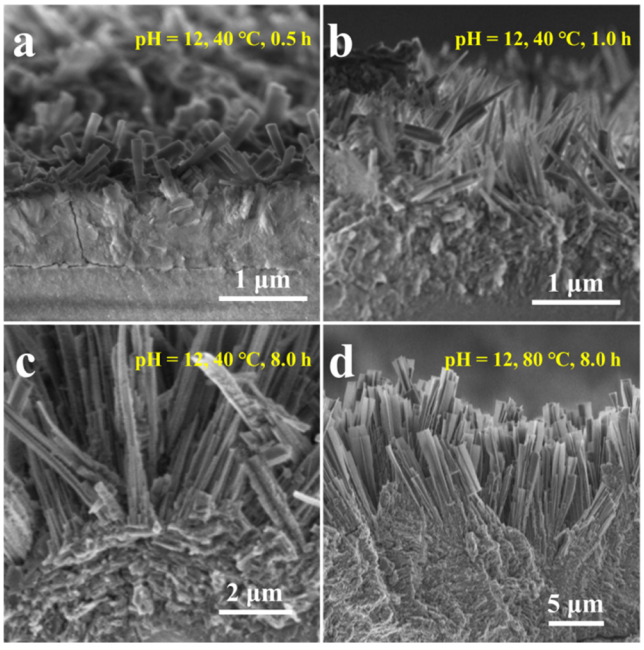

Figure 8. SEM of cross-section of oxidation Al foam with pH = 12 (the reaction times of a, b, and c are different; the reaction times of c and d are different.)

4. CONCLUSIONS

We have shown a simple method for the *in situ* development of γ-Al_2O_3 nanowire arrays on Al foam using an alkaline solution, making the manufacture of monolithic catalysts more reliable. In addition, γ-Al_2O_3 nanowires loaded with Pt metals are applied for C_2H_4 catalytic oxidation. Because of its hierarchical structure, Pt/AlO exhibits high activity and thermal stability for C_2H_4 oxidation under dry conditions as well as in water vapor (5, 10, and 15% volume percent). For the first time, the

https://doi.org/10.1021/acsomega.2c07237
ACS Omega 2023, 8, 1643−1651

new-type γ-Al_2O_3 material is manufactured as regular nanowires with higher energy $(\bar{1}\bar{1}2)$ and $(\bar{1}2\bar{1})$ facets, which have higher density of atomic steps and kinks interacting aggressively with supported noble metals. As a result, the Pt-loaded oxidation Al foam used in this study exhibits the benefits of lightweight, high mechanical resilience, ease of manipulation, uniform distribution of temperature, and strong adherence to the Al substrate. Overall, the Pt-loaded oxide Al foam is projected to be an efficient and scalable monolithic catalyst in VOC treatment.

■ ASSOCIATED CONTENT

Supporting Information

The Supporting Information is available free of charge at https://pubs.acs.org/doi/10.1021/acsomega.2c07237.

EDS analytical data and SEM and EDS mapping images (PDF)

■ AUTHOR INFORMATION

Corresponding Author

Baodong Wang − *National Institute of Clean-and-Low-Carbon Energy, Beijing 102211, China;* orcid.org/0000-0002-2113-8020; Email: baodong.wang.d@chnenergy.com.cn

Authors

Shengpan Peng − *National Institute of Clean-and-Low-Carbon Energy, Beijing 102211, China;* orcid.org/0000-0003-2770-5660

Ziran Ma − *National Institute of Clean-and-Low-Carbon Energy, Beijing 102211, China*

Jing Ma − *National Institute of Clean-and-Low-Carbon Energy, Beijing 102211, China*

Zhihua Han − *National Institute of Clean-and-Low-Carbon Energy, Beijing 102211, China*

Hongyan Wang − *National Institute of Clean-and-Low-Carbon Energy, Beijing 102211, China*

Feng Zhao − *Institute of Process Engineering, Chinese Academy of Sciences, Beijing 100190, China*

Ge Li − *National Institute of Clean-and-Low-Carbon Energy, Beijing 102211, China*

Complete contact information is available at: https://pubs.acs.org/10.1021/acsomega.2c07237

Author Contributions

[§]S.P. and Z.M. contributed equally to this work.

Notes

The authors declare the following competing financial interest(s): The authors have filed patent applications for the synthesis of a monolithic catalyst for aluminum foam.

The authors have filed patent applications for the synthesis of a monolithic catalyst for aluminum foam.

■ ACKNOWLEDGMENTS

This work was supported by the Science and Technology Project of China Energy Investment, which is the development and engineering demonstration of key materials for VOC oxidation catalysis in the coal chemical industry (ST930021005C).

■ ABBREVIATIONS

EDSenergy dispersive spectroscopy; FT-IRFourier transform infrared reflection; GHSVgas hourly space velocity; HAADF-high-angle annular dark-field; IPCCIntergovernmental Panel on Climate Change; LDHslayered double hydroxides; MCTsmercury−cadmium−telluride; RCOregenerative catalytic oxidation; SAEDselected area electron diffraction; SEMscanning electron microscope; STEMsscanning transmission electron microscope; TEMtransmission electron microscopy; VOCsvolatile organic compounds; XRDX-ray diffraction; γ-AlOOHboehmite

■ REFERENCES

(1) Zhang, Q.; Zheng, Y.; Tong, D.; Shao, M.; Wang, S.; Zhang, Y.; Xu, X.; Wang, J.; He, H.; Liu, W.; Ding, Y.; Lei, Y.; Li, J.; Wang, Z.; Zhang, X.; Wang, Y.; Cheng, J.; Liu, Y.; Shi, Q.; Yan, L.; Geng, G.; Hong, C.; Li, M.; Liu, F.; Zheng, B.; Cao, J.; Ding, A.; Gao, J.; Fu, Q.; Huo, J.; Liu, B.; Liu, Z.; Yang, F.; He, K.; Hao, J. Drivers of improved $PM_{2.5}$ air quality in China from 2013 to 2017. *Proc. Natl. Acad. Sci. U.S.A.* **2019**, *116*, 24463−24469.

(2) Sun, W.; Shao, M.; Granier, C.; Liu, Y.; Ye, C. S.; Zheng, J. Y. Long-term trends of anthropogenic SO_2, NOx, CO, and NMVOCs emissions in China. *Earth's Future* **2018**, *6*, 1112−1133.

(3) He, C.; Cheng, J.; Zhang, X.; Douthwaite, M.; Pattisson, S.; Hao, Z. P. Recent advances in the catalytic oxidation of volatile organic compounds: A review based on pollutant sorts and sources. *Chem. Rev.* **2019**, *119*, 4471−4568.

(4) Laurell, M.; Sjörs, J.; Wernlund, B.; Brück, R. Commonised diesel and gasoline catalyst architecture. *MTZ Worldwide* **2013**, *74*, 30−35.

(5) Lambert, C. K. Current state of the art and future needs for automotive exhaust catalysis. *Nat. Catal.* **2019**, *2*, 554−557.

(6) Almohamadi, H.; Alamoudi, M. A.; Smith, K. J. Washcoat overlayer for improved activity and stability of natural gas vehicle monolith catalysts operating in the presence of H_2O and SO_2. *Ind. Eng. Chem. Res.* **2021**, *60*, 3572−3580.

(7) Benu, D. P.; Hardian, A.; Mukti, R. R.; Yuliarto, B.; Fukumitsu, N.; Ide, Y.; Yamauchi, Y.; Kaneti, Y. V.; Suendo, V. Reverse micelle-mediated synthesis of plate-assembled hierarchical three-dimensional flower-like gamma-alumina particles. *Microporous Mesoporous Mater.* **2021**, *321*, No. 111055.

(8) Trueba, M.; Trasatti, S. P. γ-Alumina as a support for catalysts: A review of fundamental aspects. *Eur. J. Inorg. Chem.* **2005**, *2005*, 3393−3403.

(9) Kumar, A.; Mazumder, S. Toward simulation of full-scale monolithic catalytic converters with complex heterogeneous chemistry. *Comput. Chem. Eng.* **2010**, *34*, 135−145.

(10) Hirose, S.; Yamamoto, H.; Suenobu, H.; Sakamoto, H.; Katsube, F.; Busch, P.; Martin, A.; Kai, R.; Vogt, C. D. Development of high porosity cordierite honeycomb substrate for SCR application to realize high NOx conversion efficiency and system compactness. *SAE Int. J. Mater. Manuf.* **2014**, *7*, 682−687.

(11) Seong, H.; Choi, S.; Matusik, K. E.; Kastengren, A. L.; Powell, C. F. 3D pore analysis of gasoline particulate filters using X-ray tomography: Impact of coating and ash loading. *J. Mater. Sci.* **2019**, *54*, 6053−6065.

(12) von Rickenbach, J.; Lucci, F.; Narayanan, C.; Eggenschwiler, P. D.; Poulikakos, D. Effect of washcoat diffusion resistance in foam based catalytic reactors. *Chem. Eng. J.* **2015**, *276*, 388−397.

(13) Mladenov, N.; Koop, J.; Tischer, S.; Deutschmann, O. Modeling of transport and chemistry in channel flows of automotive catalytic converters. *Chem. Eng. Sci.* **2010**, *65*, 812−826.

(14) Xue, T.; Li, R.; Gao, Y.; Wang, Q. Iron mesh-supported vertically aligned Co-Fe layered double oxide as a novel monolithic catalyst for catalytic oxidation of toluene. *Chem. Eng. J.* **2020**, *384*, No. 123284.

(15) Xu, K.; Wang, Z.; He, C.; Ruan, S.; Liu, F.; Zhang, L. Flame in situ synthesis of metal-anchored CuO nanowires for CO catalytic oxidation and kinetic analysis. *ACS Appl. Energy Mater.* **2021**, *4*, 13226−13238.
(16) Giani, L.; Groppi, G.; Tronconi, E. Mass transfer characterization of metallic foams as supports for structured catalysts. *Ind. Eng. Chem. Res.* **2005**, *44*, 4993−5002.
(17) Gong, S.; Wang, A.; Wang, Y.; Liu, H.; Han, N.; Chen, Y. Heterostructured Ni/NiO nanocatalysts for ozone decomposition. *ACS Appl. Nano Mater.* **2020**, *3*, 597−607.
(18) He, S.; Zhao, Y.; Wei, M.; Evans, D. G.; Duan, X. Fabrication of hierarchical layered double hydroxide framework on aluminum foam as a structured adsorbent for water treatment. *Ind. Eng. Chem. Res.* **2012**, *51*, 285−291.
(19) Saptiama, I.; Kaneti, Y. V.; Yuliarto, B.; Kumada, H.; Tsuchiya, K.; Fujita, Y.; Malgras, V.; Fukumitsu, N.; Sakae, T.; Hatano, K.; Ariga, K.; Sugahara, Y.; Yamauchi, Y. Biomolecule-assisted synthesis of hierarchical multilayered boehmite and alumina nanosheets for enhanced molybdenum adsorption. *Chem. - Eur. J.* **2019**, *25*, 4843−4855.
(20) Kodama, T.; Kiyama, A.; Shimizu, K. I. Catalytically activated metal foam absorber for light-to-chemical energy conversion via solar reforming of methane. *Energy Fuels* **2003**, *17*, 13−17.
(21) Zhang, S.; Yang, Z.; Cui, C.; Chen, X.; Yu, Y.; Qian, W.; Jin, Y. Ultrafast nonvolatile ionic liquids-based supercapacitors with Al foam-enhanced carbon electrode. *ACS Appl. Mater. Interfaces* **2021**, *13*, 53904−53914.
(22) Kim, H. W.; Bae, J. K.; Kang, M. G.; Jang, S. C.; Ham, H. C.; Yoon, S. P.; Choi, H. J. Effect of oxidation on the Al-foam reinforced matrix for molten carbonate fuel cells. *Int. J. Hydrogen Energy* **2019**, *44*, 22210−22217.
(23) Jiang, J.; Zhu, Y.; Ma, A.; Yang, D.; Lu, F.; Chen, J.; Shi, J.; Song, D. Preparation and performances of bulk porous Al foams impregnated with phase-change-materials for thermal storage. *Prog. Nat. Sci.: Mater. Int.* **2012**, *22*, 440−444.
(24) Mei, X.; Zhu, X.; Zhang, Y.; Zhang, Z.; Zhong, Z.; Xin, Y.; Zhang, J. Decreasing the catalytic ignition temperature of diesel soot using electrified conductive oxide catalysts. *Nat. Catal.* **2021**, *4*, 1002−1011.
(25) Chen, Y.; Sima, V.; Lin, W. Y.; Sterniak, J.; Bohac, S. V. Lean HCCI/Rich SACI gasoline combustion cycling and three-way catalyst for fuel efficiency and NOx reduction. *J. Eng. Gas Turbines Power* **2015**, *137*, No. 121508.
(26) Valette, A.; Corral Valero, M.; Lefèvre, G.; Vallée, C.; Digne, M.; Humbert, S.; Chanéac, C.; Durupthy, O. Interplay of solid-liquid interactions and anisotropic aggregation in solution: The case study of γ-AlOOH crystallites. *J. Phys. Chem. C* **2021**, *125*, 26049−26060.
(27) Li, Z.; Liu, G. H.; Li, X. B.; Qi, T.; Peng, Z. H.; Zhou, Q. S. Effects of cation on the morphology of boehmite precipitated from alkaline solutions by adding gibbsite as seed. *Cryst. Growth Des.* **2019**, *19*, 1778−1785.
(28) Yu, N. F.; Tian, N.; Zhou, Z. Y.; Huang, L.; Xiao, J.; Wen, Y. H.; Sun, S. G. Electrochemical synthesis of tetrahexahedral rhodium nanocrystals with extraordinarily high surface energy and high electrocatalytic activity. *Angew. Chem., Int. Ed.* **2014**, *53*, 5097−5101.
(29) Fehlner, F. P.; Mott, N. F. Low-Temperature Oxidation. *Oxid. Met.* **1970**, *2*, 59−99.
(30) Kuzik, L. A.; Yakovlev, V. A. Effect of a noble metal coating on a natural aluminum oxide film. *Thin Solid Films* **1999**, *340*, 288−291.
(31) Zhang, Z. R.; Hicks, R. W.; Pauly, T. R.; Pinnavaia, T. J. Mesostructured forms of gamma-Al_2O_3. *J. Am. Chem. Soc.* **2002**, *124*, 1592−1593.
(32) Xu, S.; Jaegers, N. R.; Hu, W.; Kwak, J. H.; Bao, X.; Sun, J.; Wang, Y.; Hu, J. Z. High-field one-dimensional and two-dimensional (27)Al magic-angle spinning nuclear magnetic resonance study of theta-, delta-, and gamma-Al_2O_3 dominated aluminum oxides: Toward understanding the Al sites in gamma-Al_2O_3. *ACS Omega* **2021**, *6*, 4090−4099.
(33) Szczesniak, B.; Choma, J.; Jaroniec, M. Facile mechanochemical synthesis of highly mesoporous gamma-Al_2O_3 using boehmite. *Microporous Mesoporous Mater.* **2021**, *312*, 10792.
(34) Kovarik, L.; Bowden, M.; Szanyi, J. High temperature transition aluminas in δ-Al_2O_3/θ-Al_2O_3 stability range: Review. *J. Catal.* **2021**, *393*, 357−368.
(35) Zhang, X.; Cui, W. W.; Page, K. L.; Pearce, C. I.; Bowden, M. E.; Graham, T. R.; Shen, Z. Z.; Li, P.; Wang, Z. M.; Kerisit, S.; N'Diaye, A. T.; Clark, S. B.; Rosso, K. M. Size and morphology controlled synthesis of boehmite nanoplates and crystal growth mechanisms. *Cryst. Growth Des.* **2018**, *18*, 3596−3606.
(36) Cai, W. M.; Zhang, S. G.; Lv, J. G.; Chen, J. C.; Yang, J.; Wang, Y. B.; Guo, X. F.; Peng, L. M.; Ding, W. P.; Chen, Y.; Lei, Y. H.; Chen, Z. X.; Yang, W. M.; Xie, Z. K. Nanotubular gamma Alumina with high-energy external surfaces: Synthesis and high performance for catalysis. *ACS Catal.* **2017**, *7*, 4083−4092.
(37) Jiao, W.; Wu, X.; Xue, T.; Li, G.; Wang, W.; Wang, Y.; Wang, Y.; Tang, Y.; He, M. Y. Morphological controlled growth of nanosized boehmite with enhanced aspect ratios in an organic additive-free cationic-Anionic double hydrolysis method. *Cryst. Growth Des.* **2016**, *16*, 5166−5173.
(38) Lebedeva, N. P.; Koper, M. T. M.; Feliu, J. M.; Santen, R. A. V. Role of crystalline defects in electrocatalysis: Mechanism and kinetics of CO adlayer oxidation on stepped platinum electrodes. *J. Phys. Chem. B* **2002**, *106*, 12938−12947.
(39) Tian, N.; Zhou, Z. Y.; Sun, S. G. Platinum metal catalysts of high-index surfaces: From single-crystal planes to electrochemically shape-controlled nanoparticles. *J. Phys. Chem. C* **2008**, *112*, 19801−19817.
(40) Kwak, J. H.; Hu, J. Z.; Mei, D.; Yi, C. W.; Kim, D. H.; Peden, C. H. F.; Allard, L. F.; Szanyi, J. Coordinatively unsaturated Al^{3+} centers as binding sites for active catalyst phases of platinum on gamma-Al_2O_3. *Science* **2009**, *325*, 1670−1673.
(41) Barsotti, E.; Piri, M. Effect of pore size distribution on capillary condensation in nanoporous media. *Langmuir* **2021**, *37*, 2276−2288.
(42) Bunker, B. C.; Nelson, G. C.; Zavadil, K. R.; Barbour, J. C.; Wall, F. D.; Sullivan, J. P.; Windisch, C. F.; Engelhardt, M. H.; Baer, D. R. Hydration of passive oxide films on aluminum. *J. Phys. Chem. B* **2002**, *106*, 4705−4713.
(43) Sohlberg, K.; Stephen, J. P.; Sokrates, T. P. Hydrogen and the structure of the transition aluminas. *J. Am. Chem. Soc.* **1999**, *121*, 7493−7499.
(44) Maurice, V.; Despert, G.; Zanna, S.; Bacos, M. P.; Marcus, P. Self-assembling of atomic vacancies at an oxide/intermetallic alloy interface. *Nat. Mater.* **2004**, *3*, 687−691.
(45) Urbonavicius, M.; Varnagiris, S.; Pranevicius, L.; Milcius, D. Production of gamma alumina using plasma-treated aluminum and water reaction byproducts. *Materials* **2020**, *13*, No. 1300.
(46) Deng, Z.; Liu, Y.; Tanaka, Y.; Ye, J.; Sakka, Y. Modification of Al particle surfaces by γ-Al_2O_3 and its effect on the corrosion behavior of Al. *J. Am. Ceram. Soc.* **2005**, *88*, 977−979.
(47) Deng, Z. Y.; Ferreiraw, J. M. F.; Tanaka, Y.; Ye, J. Physicochemical mechanism for the continuous reaction of gamma-Al_2O_3-modified aluminum powder with water. *J. Am. Ceram. Soc.* **2007**, *90*, 1521−1526.

https://doi.org/10.1021/acsomega.2c07237
ACS Omega 2023, 8, 1643−1651